The Effect of Cell Geometry and Trigger Mechanism on the Risks Associated with Thermal Runaway of Lithium-ion Batteries: Part 1 Comparative Analysis of Thermal Runaway Heat Output Variability

William Q. Walker[a]*, Kylie Cooper[b], Peter Hughes[a], Ian Doemling[b], Mina Akhnoukh[c], Sydney Taylor[a], Jacob Darst[a], Julia Billman[d], Matthew Sharp[d], David Petrushenko[a], Rhodri Owen[e], Martin Pham[e], Thomas Heenan[e], Alexander Rack[f], Oxana Magdsyuk[g], Thomas Connolley[g], Paul Shearing[e], Donal Finegan[d]*, Eric Darcy[a]

[a]*National Aeronautics and Space Administration (NASA) Johnson Space Center (JSC), 2101 NASA Parkway, Houston, TX 77058, USA*
[b]*Universities Space Research Association (USRA), 7178 Columbia Gateway Drive, Columbia, MD 21046, USA*
[c]*Jacobs, 1999 Bryan Street, Suite 1200, Dallas, TX 75201, USA*
[d]*National Renewable Energy Laboratory (NREL), 15013 Denver West Parkway, Golden, CO 80501, USA*
[e]*University College London (UCL), Gower St, Bloomsbury, London WC1E 6BT, UK*
[f]*European Synchrotron Radiation Facility (ESRF), 71 Avenue des Martyrs, 38000 Grenoble, FR*
[g]*Diamond Light Source (DLS), Harwell Science and Innovation Campus, Fermi Ave, Didcot OX11 0DE, UK*
**Corresponding Authors: william.walker@nasa.gov; donal.finegan@nrel.gov*

Lithium-ion (Li-ion) batteries are a popular energy storage solution utilized across industries for their high specific and volumetric energy density. With a range of formats and designs for both high power and high energy applications, Li-ion cells are versatile and configurable. Despite their widespread popularity, there are major safety concerns regarding their potential for hazardous thermal runaway events. The possibility of catastrophic failures necessitates safe battery design with robust thermal management systems. However, to achieve these goals often complex thermal modelling and extensive abuse testing campaigns are required to certify batteries for use in an application. There is a need to understand the impacts of trigger mechanism and cell format on thermal runaway heat output in order to improve testing capabilities and better inform thermal models. This study examines thermal runaway heat output for three different cell formats as a function of trigger mechanism. The cell formats considered are 18650, 21700, and D-cell. The trigger mechanisms considered are heaters, internal short circuiting device, and nail penetration. Specifically, the thermal runaway responses for the KULR 18650-K330, KULR 21700-K500, LG 21700-M50, and Saft D-Cell-VES16 are examined. All experiments are conducted inside a Fractional Thermal Runaway Calorimeter (FTRC). The FTRC data, which is stored in the Battery Failure Databank, is extracted and analyzed to provide a comparative analysis of thermal runaway heat output as a function of trigger mechanism and cell format based on the calculated total energy yield, fractional energy yield, heat rate, and heat flux. By analyzing the variability between experiments in these values, this study seeks to demonstrate relationships between thermal runaway heat output, cell format, and initiation method to aid in the development of future abuse tests and modeling methods.

1. Introduction

Lithium-ion (Li-ion) cell technology offers high specific and volumetric energy density storage solutions for various industry sectors [1]. With a range of formats and designs for both high power and high energy applications, Li-ion cells are versatile and configurable. Despite their widespread popularity, there are significant safety concerns regarding their safety due to violent thermal runaway events and studies continue to focus on new and innovative methods to characterize thermal runaway via test, simulate thermal runaway via models, stop thermal runaway with devices constructed inside of the cell, and to protect against thermal runaway with advanced thermal management systems [2–5]. Such concerns are heightened in the automotive, aerospace, and space industries, where failures can endanger human lives [4,6–10].

Thermal runaway is a failure mode in Li-ion cells that occurs when the temperature of the cell, or area within the cell, exceeds a threshold value, which induces the onset of exothermic decomposition [2,11,12]. Arrhenius form self-heating begins when the cell's internal self-heating rate exceeds its external heat dissipation rate [2,11,12]; eventually, stability is lost and heat, hot gases, and molten ejecta are then violently and rapidly expelled from the cell [2,11,12]. Additionally, there are four primary categories of triggers that can induce thermal runaway in a Li-ion cell in a test or field environment: thermal failure (e.g. overheating), mechanical failure (e.g. nail penetration or crushing of the cell casing), short circuiting (e.g. internal and external), and electro-chemical abuse (e.g. overcharge and over-discharge) [2,11,13,14]. Cell-to-cell propagation is also a concern in instances when Li-ion cells are connected in series and parallel to form larger packs, modules, and assemblies. Cell-to-cell propagation refers to when the effects of one cell going into thermal runaway forces neighbor cells into a thermal runaway condition; this is a dangerous scenario that can result in thermal runaway cascading through the battery system that does not stop until all cells have undergone thermal runaway [15–18].

The potential for such catastrophic failures necessitates safe battery design with robust thermal management systems. However, to achieve these goals complex thermal modelling and extensive abuse testing campaigns are often required to certify cells and battery assemblies for usage in their intended applications. Designing a rigorous testing campaign or producing a useful thermal model is no trivial matter. Numerous variables can impact the response of the thermal runaway event including; trigger mechanism, cell format, cell chemistry, power cell vs. energy cell behavior, nominal vs. off-nominal cell failure modes, mechanical design features such as venting mechanisms and casing thickness, and built-in safety devices such as current interrupt devices [11,19–21]. Additional complexity is added when considering that no two thermal runaway events are the same, even when the same cell, at the same state of charge, with the same trigger mechanism is tested; there is always a level of variability on an event to event basis [11,19–21].

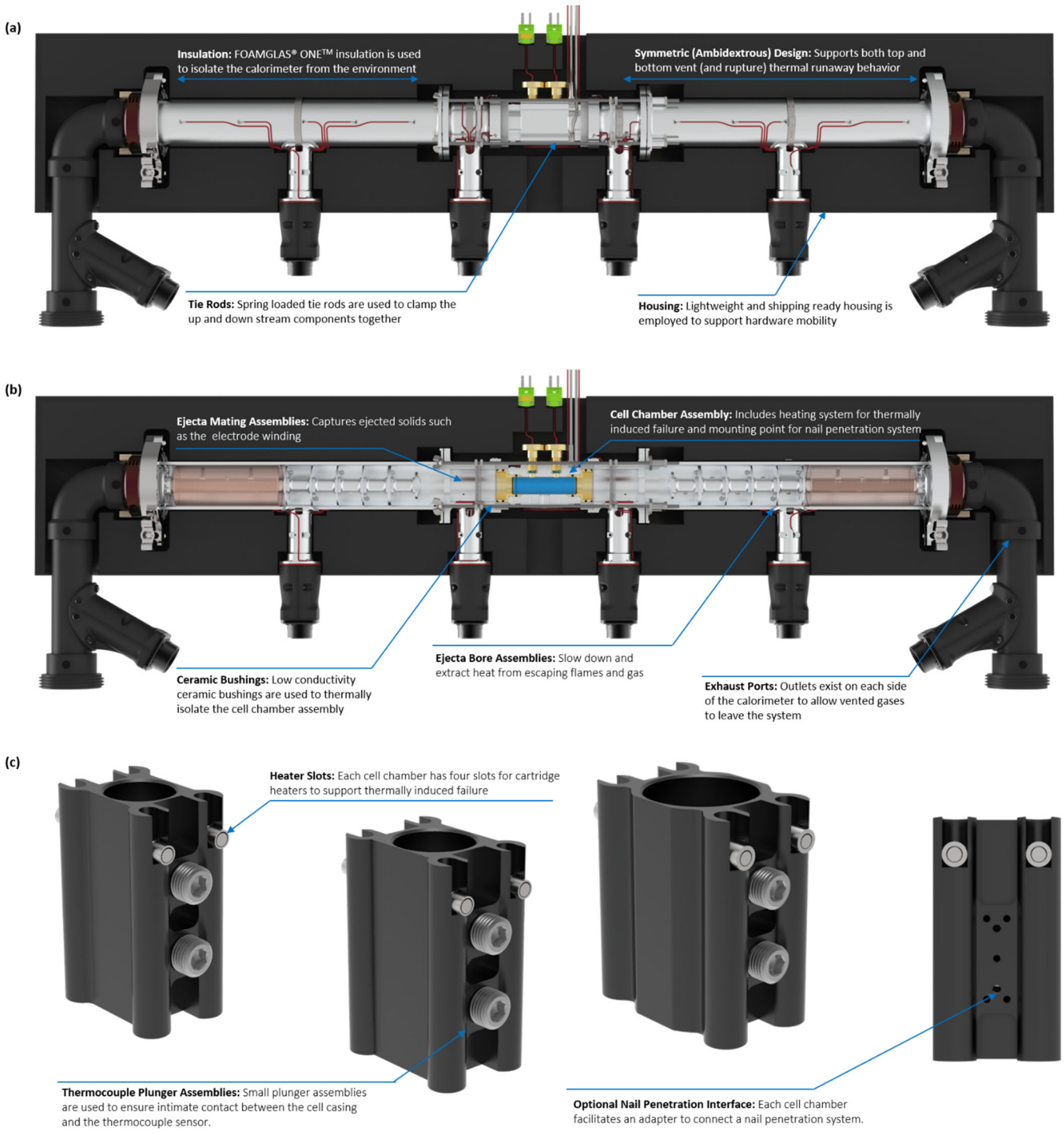

Fig 1 Rendered images of the fractional thermal runaway calorimeter (FTRC) where (a) identifies the fractional calorimeter exterior with the housing and FOAMGLAS® ONE™ insulation, the tie rod assemblies, and the symmetric design highlighted, (b) uses a cutaway view to highlight the primary FTRC sub-assemblies, ceramic bushings, and exhaust ports, and where (c) depicts the three different cell chambers (i.e. 18650, 21700, and D-Cell) and their key features. Note that the device as depicted with (a) and (b) is ambidextrous to support cells with both top and bottom vents where bottom vent cells can experience rupture from both ends of the cell; this design also accommodates top vent cells experiencing a breach at the bottom of the cell.

Considering the expansive list of relevant factors that can influence Li-ion cell thermal runaway response, battery designers may find difficulty in interpreting the results of a given abuse test, whether cell level or assembly level, or the results of an extensive thermal analysis if the overall range of cell level thermal runaway behavior for the trigger cell and trigger mechanism configuration is not first understood. Recall that no two thermal runaway events are the same, thus it is the battery designer's responsibility to understand where their test and analysis results stand as they pertain to the overall range of possible behaviors for the trigger cell and trigger mechanism configuration. Therefore, we recommend beginning with comprehensive cell level thermal runaway characterization via calorimetric means to become better informed

Table 1 Describes cells and trigger mechanisms considered, and the quantities of cells tested per trigger mechanism.

Cell Description	Capacity	Nominal Voltage	Stored Energy	Surface Area	Bottom Vent (Yes/No)	Heater (ISC) Trigger[1]	Heater (Non-ISC) Trigger[1]	Nail Pen. Trigger[1]
KULR 18650-K330	3.3 A-h	3.6 V	11.88 W-h	41.83 cm^2 (0.004183 m^2)	Yes	Yes (9)	Yes (10)	Yes (3)
KULR 21700-K500	5.0 A-h	3.6 V	18.0 W-h	46.16 cm^2 (0.004616 m^2)	Yes	Yes (10)	Yes (6)	Yes (11)
LG 21700-M50	5.01 A-h	3.63 V	18.2 W-h	46.16 cm^2 (0.004616 m^2)	Yes	No (0)[2]	Yes (7)	Yes (5)
Saft D-Cell-VES16	4.5 A-h	3.6 V	16.2 W-h	79.28 cm^2 (0.007928 m^2)	No	Yes (9)	Yes (9)	Yes (9)

[1] *The number in parenthesis in these columns represents the number of experiments conducted for the trigger mechanism.*
[2] *Note that LG 21700-M50 cells with ISC installed were not available for this series of experiments.*

about a given cell's safety performance prior to the costly and time consuming process of designing and evaluating battery assembly level response to thermal runaway. Using an approach that starts with comprehensive cell level abuse test data sets, such as those presented by Walker et. al. [11] can offer effective solutions to the aforementioned challenges and ultimately result in accurate thermal runaway models and improved battery designs with higher safety margins.

Therefore, there is a need to understand the impacts of relevant variables on thermal runaway response in order to improve testing capabilities and better inform thermal models. This study provides a comparative analysis of thermal runaway heat output as a function of trigger mechanism and cell format. The cell formats considered are 18650 (~18mm diameter and 65mm height), 21700 (~21mm diameter and 70mm height), D-cell (~33mm diameter and 60mm height). The trigger mechanisms considered are cartridge heaters, cartridge heaters plus an *internal short circuiting (ISC)* device, and nail penetration. The ISC device is a small lay-up of current collector, electrode and separator materials with an internal copper puck that is ensconced in a wax phase change material that melts at low temperature (~50 °C); when the wax melts the copper puck creates an electrical connection between the positive and negative current collectors and thus results in the short circuiting of the cell [22]. The ISC device is pre-assembled and installed in the Li-ion cell during the manufacturing process and provides a reliable means for producing internal short circuit induced thermal runaway events in a controlled and repeatable manner [22].

Specifically, the total and fractional thermal runaway heat output for the KULR 18650-K330, KULR 21700-K500, LG 21700-M50, and Saft D-Cell-VES16 are examined using a technique described as fractional calorimetry with a calorimetric tool that is referred to as the *Fractional Thermal Runaway Calorimeter (FTRC)* or *fractional calorimeter*; see Fig 1. Table 1 describes the performance characteristics of each cell type and the number of experiments conducted per trigger mechanism inside of the FTRC. The data gathered from the FTRC experiments are stored in the Battery Failure Databank, a publicly accessible utility provided by the National Aeronautics and Space Administration (NASA) and the National Renewable Energy Laboratory (NREL), that stores data gathered from 300+ thermal runaway experiments [23]. The databank is a two component system with the first component being a set of tabular formatted FTRC data (e.g. experiment specific total energy release, fractional energy release, and ejected mass distributions) and the second component being a radiographic video library containing high speed x-ray videos (~1700-2000 fps) gathered from combination FTRC-synchrotron experiments; note that the synchrotron experiments were conducted at both the European Synchrotron Radiation Facility (ESRF) in France and at Diamond Light Source (DLS) in the United Kingdom (UK). Fig 2a displays the FTRC on the test stand at DLS and illustrates the X-ray beam that was used to generate the X-ray images that are captured with a high speed camera as shown with Fig 2b. The Battery Failure Databank aims to provide researchers with a comprehensive dataset describing cell level thermal runaway behavior in a format conducive to linking internal phenomena to external risks.

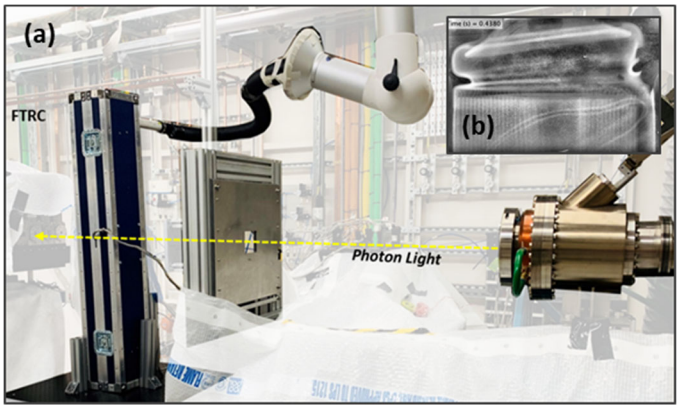

Fig 2 Depicts the FTRC in the testing configuration at Diamond Light Source (DLS) where (a) shows the calorimeter on the test stand where it is imaged using X-rays to generate radiographs and (b) displays an example radiograph that was collected via a high speed camera in-situ during the combination FTRC-synchrotron experiments

The data considered for this study for the aforementioned cell types and trigger mechanisms are extracted from the databank and used to perform a comparative analysis in the variability of thermal runaway heat output as a function of trigger mechanism and cell format. The analysis is based on experiment specific total energy yield (kJ), fractional energy yield (kJ), heat rate (W), and heat flux (W m^{-2}). Discussion is also provided on the approximation of the length of the thermal runaway event (s) which is required for heat flux and heat rate calculations. By analyzing the variability in the values between each experiment, this study seeks to demonstrate relationships between thermal runaway heat output, cell format, and initiation method to aid in the development of future abuse tests and modeling methods.

2. Literature Review

Prior to describing the details of this study, it is first essential to provide description of the findings of other calorimetric studies reported in literature that are focused on characterization of Li-ion cell thermal runaway heat output. Results from other studies that utilize forms of fractional thermal runaway calorimetry, accelerating rate calorimetry, bomb calorimetry, copper slug calorimetry, and cone calorimetry are described in this section.

Walker et. al. provides the first detailed study focused on heat output for experiments conducted with fractional calorimetry [11]. This study sought to examine the thermal runaway behavior of 18650-format Li-ion cells with various manufacturers, chemistries, capacities, and safety features [11]. The experiments conducted by Walker et. al. were conducted with Li-ion cells charged to 100% state-of-charge (SOC). The FTRC supported the discernment between total energy yield and the fractions of energy as they are released through the cell casing and ejecta [11]. The cells considered in this investigation included the 3.5 A-h LG 18650-MJ1, 3.35 A-h LG 18650 test cell (BV-220), 3.35 Ah LG 18650 test cell (non-BV 220), 3.0 A-h Samsung 18650-30Q, 2.4 A-h MOLiCEL®

18650-J (polymer separator) and 2.4 A-h MOLiCEL® 18650-J (Dreamweaver separator) [11]. The LG 18650-MJ1 cells output the highest thermal runaway energy, averaging 75.2 kJ per trial [11]. The lowest observed thermal runaway energy resulted from testing the MOLiCEL® 18650-J batteries with the standard polymer separator, which was relatively low at 36.2 kJ [11]. A regression analysis was conducted in parallel to determine the statistical expectations for total thermal runaway energy release based on various control variables. The predicted median for total energy output was within 5% of the observed averages for each of the five cell types tested [11].

Lyon et. al. incorporated bomb calorimetry testing when examining the heat output of four fully charged 18650-format batteries, all of which had varying cathode chemistries [24]. These chemistries included $LiNiCoAlO_2$ (NCA), $LiCoO_2$, $LiMN_2O_4$-$LiNiCoO_2$, and an unknown material. The testing apparatus consisted of a nitrogen-filled pressure vessel and electrical resistance heating to induce thermal runaway, with heat tests generally lasting for a span of 15 minutes [24]. An increasing fractional charge in the batteries generally exhibited greater reaction energies, although a drop-off in reaction energy occurred for some batteries when fully charged [24]. The largest reaction energy recorded for the experiment was 34.8 kJ, occurring in $LiMn_2O_4$-$LiNiCoO_2$ cells at a fractional charge of 67% [24]. This cathode chemistry exhibited the highest reaction energies among all batteries for the various fractional charges tested [24]. The unknown and $LiNiCoAlO_2$ cathode chemistries output the least energy, producing 11.0 kJ and 16.3 kJ for fractional charges of 59% and 100%, respectively [24].

Zhao et. al. investigated the thermal properties of Li-ion batteries using a bomb calorimeter that was placed inside an extended volume accelerating rate calorimeter [25]. This bomb calorimeter portion of the apparatus included a stainless-steel canister equipped with six ports for measuring temperature, pressure, voltage, etc. [25]. Trends for pressure and temperature showed that cells at higher SOC display greater surface temperatures and canister internal pressures during thermal runaway [25]. Similarly, the total energy of the cell and canister apparatus tended to peak at 100% SOC [25]. As the SOC decreased to 25%, the total energy output decreased approximately 67% from 60 kJ to 20 kJ [25]. Cells cycled hundreds of times to an SOC of 100% tended to have a drop off in energy, exhibiting between 45 and 55 kJ of total energy [25]. This was roughly the equivalent of fresh cells at states of charge ranging from 75% to 85% [25].

Golubkov et. al. examined the impact of various states of charge and overcharge on the thermal runaway phenomena occurring in 18650-format Li-ion batteries with $LiFePO_4$ (LFP) and NCA cathodes [26]. Discharged NCA cell showed no sign of thermal runaway when tested. However, SOCs as low as 25% exhibited clear thermal runaway behavior [26]. These partially charged NCA cells displayed self-accelerating exothermic reactions that resulted in peak temperatures ranging from 739 °C to 1075 °C [26]. Overcharged NCA cells provided the greatest hazard, however, as thermal runaway was observed at a threshold temperature of 65 °C. These batteries also produced more vent-gas when undergoing thermal runaway at higher states of charge (up to 317 mmol) [26]. The tests conducted on LFP cells displayed no thermal runaway when fully discharged, similar to the NCA cells [26]. However, thermal runaway reactions in LFP cells occurred at a bottom threshold of 50% SOC [26]. The self-accelerating exothermic reactions for this cell type ranged in temperature from 283 °C to 448 °C [26]. Overcharged LFP cells were able to go into sustainable thermal runaway at temperatures significantly higher than NCA cells, reaching the state at 140 °C [26]. Additionally, the peak amount of gas ejected from NCA cells was approximately 61 mmol and did not appear to be dependent on the SOC of the cell [26].

Jhu et. al. studied the thermal runaway reactions of 18650-format Li-ion cells using a adiabatic (VSP2) calorimeter [27]. A closed test cannister (also known as a bomb cannister) was included with the calorimeter to ensure that all of the released reaction heat and pressure remained within the testing apparatus [27]. The focus of this publication was on Sony, Samsung, Sanyo, and LG cells with $LiCoO_2$ cathodes [27]. Each cell was tested at a charged state of 4.2 V and a discharged state of 3.7 V. The exothermic reaction energy for the charged cells ranged from 18.4 kJ to 26.2 kJ, while the discharged cells ranged from 8.0 kJ to 12.3 kJ. These results display a 42-54% spike in energy release when charged an additional 0.5 V [27].

Liu et. al. incorporated Copper Slug Battery Calorimetry (CSBC) to measure the dynamics of thermally induced failure of 18650-format Li-ion batteries containing LCO, NMC, and LFP cathodes [28]. These three cells were tested at 0, 25, 50, and 100% SOC to determine the heat generated by thermal runaway within the batteries [28]. The hollow cylinder (slug) of the CSBC apparatus held the Li-ion cell in place, with the top surface of each cell being level with the upper edge of the slug [28]. An electric heater composed of resistive heating wire insulated with 3 M Rubian Isolant tape was wrapped firmly around the slug [28]. This device was then used to induce and characterize thermal runaway. The results of the testing agreed with the trends found in Zhao et. al. [25], as a greater SOC resulted in higher energy output across all cell formats [28]. For a 0% SOC, the energy outputs were 8.4 kJ, 4.5 kJ, and 0.7 kJ for the LCO, NMC and LFP batteries, respectively [28]. Meanwhile, the 100% SOC energy outputs were 37.3 kJ, 34.0 kJ, and 13.7 kJ for LCO, NMC, and LFP batteries, respectively [28].

An additional experimental series was conducted by Liu et. al. using a cone calorimeter [28]. The CBSC apparatus was mounted underneath the hood of a standard cone calorimeter, with the cone heater removed due to a lack of simultaneous ignition of species ejected from all cell safety vent ports [28]. The heater was replaced by a hot wire igniter composed of a coiled OMEGA N180-010-200 resistance heating wire [28]. This device was shaped into a 22 mm diameter loop, placed 5 mm above the upper edge of the inserted Li-ion cell specimen, and obtained power from a 56 W alternating current electrical unit [28]. Due to combustion effects, the measured energy output of each cell type was significantly higher using the cone calorimeter apparatus rather than the copper slug calorimeter [28]. For a 0% SOC, the average energy outputs were 34.8 kJ, 26.8 kJ, and 49.5 kJ for LCO, NMC, and LFP batteries, respectively [28]. The average energy outputs at 100% SOC were 48.7 kJ, 64.2 kJ, and 50.0 kJ for LCO, NMC, and LFP batteries, respectively [28].

Yayathi et. al. examined the onset of thermal runaway using a accelerating rate calorimeter combined with bomb cannister [7]. This testing apparatus accounted for the distributions of energy between the cell body and gases via the inclusion the bomb cannister within the calorimeter. A set of trials was conducted on the 5.3 A-h Boston Power Swing 5300, 2.6 A-h Samsung 18650-26F, and 2.6 A-h MOLiCEL® 18650-J cells at 50 and 100% SOC. In agreement with the trends exhibited by Golubkov et. al., an increasing SOC in each battery type resulted in a lower onset temperature for thermal runaway [7]. While a 50% SOC resulted in onset temperatures ranging from 122.2 °C to 131.0 °C, the 100% SOC onset temperatures ranged from 93.4 °C to 113.9 °C [7]. Increasing the state-of-charge of each battery type, however, resulted in a profound spike in the total energy released by each cell. The Samsung 18650-26F and MOLiCEL® 18650-J cells each displayed an 88% average increase in total energy release between a 50% and 100% SOC, while the energy dissipated by the Boston Power Swing 5300 cells increased by 66% between the two states-of-charge [7].

Lammer et. al. studied the onset of thermal runaway for three types of 18650-format Lithium ion cells through thermal ramp testing [29]. The test apparatus incorporated an electric resistance furnace for housing

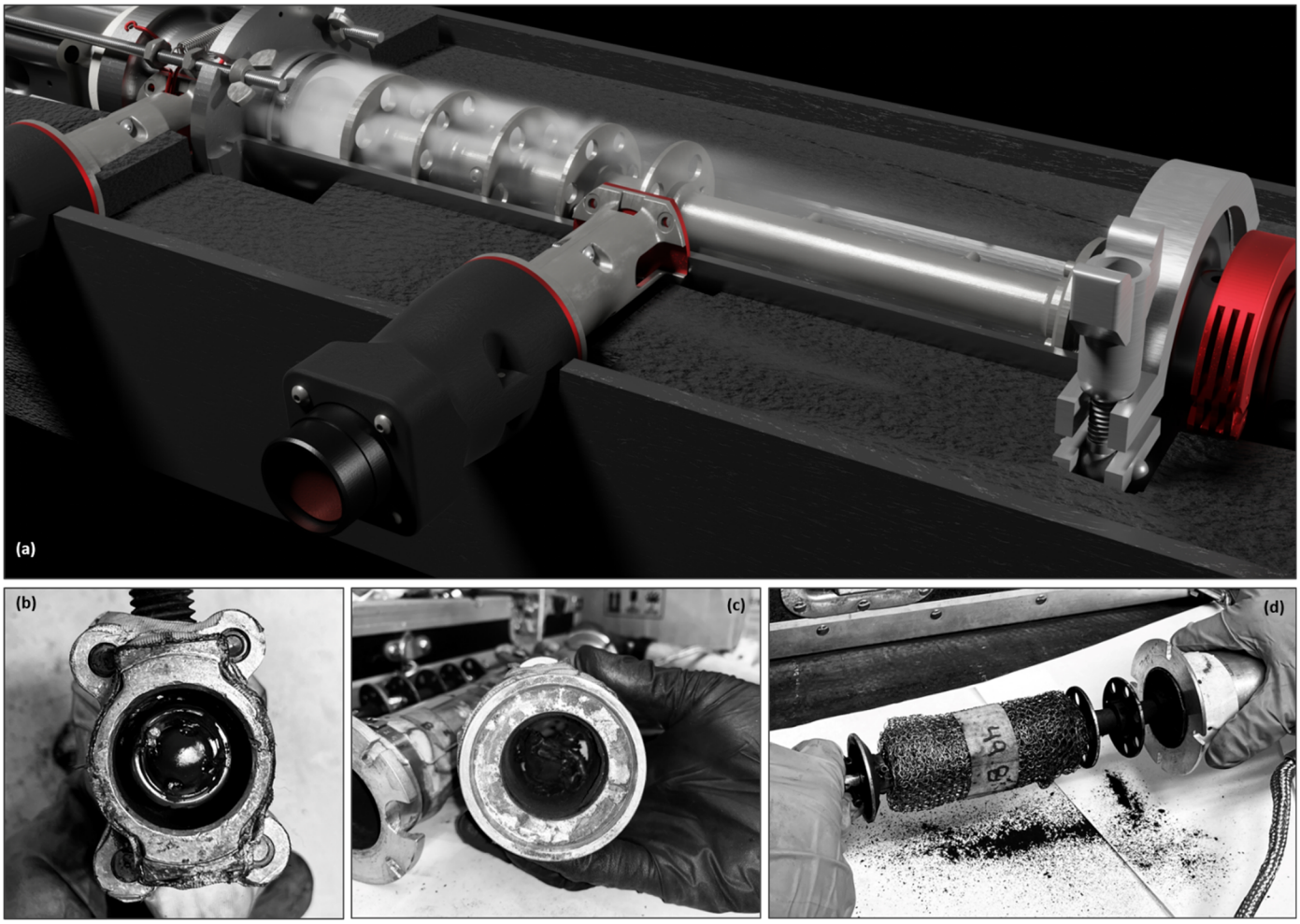

Fig 3 Image provides further depiction of how the FTRC functions where (a) displays hot ejecta flowing through the calorimeter and being decelerated by the rod and baffle assemblies and where (b)-(d) display images gathered from destructive physical analysis (DPA) of the calorimeter following an experiment where (b) shows the cell remains in the cell chamber, (c) shows the ejected electrode winding contents inside the ejecta mating, and (d) shows the ejected particulates stopped and captured by the rod and baffle assembly.

the cell, as well as thermocouples, gas inlets, pumps, and ports for collecting gas samples [29]. The three cells used for this investigation (ICR18650-32A, INR18650-35E, LG 18650-MJ1) each had similar cell chemistries and had a 100% SOC when tested [29]. The temperatures at the onset of thermal runaway ranged from 151.32 °C to 167.13 °C. With increasing onset temperature, an increase in energy released occurred [29]. The energy released by the cells ranged from 17.32 kJ to 29.49 kJ [29]. In addition to this data, the average gas emissions for each cell were accounted for [29]. The values were 129.75, 230.80, and 216.91 mmol for the ICR18650-32A, INR18650-35E, and INR18650MJ1 cells, respectively [29]. Approximately 97.5% of all emissions occurred in the deflagration phase of the tests [29].

Fu et. al. incorporated cone calorimetry into a study that measured the heat release rates of Li-ion cells [30]. Sanyo cells were loaded horizontally into a holder with a ceramic fiber blanket and wire grid encapsulating the test articles for thermal insulation [30]. The surfaces of each sample were heated up using a standard cone heater, with an exhaust hood and ventilation system installed for the collection of ejecta material and gases [30]. Cells at a 0 and 50% SOC did not undergo thermal runaway for the duration of the tests, while cells at 65, 70, and 100% SOC at an incident heat flux of 50 kW m^{-2} did experience thermal runaway at 200, 156, and 81 seconds, respectively [30]. Additionally, cells at 100% SOC had a shorter time to explosion at higher incident heat flux capacities. At incident heat fluxes of 30 kW m^{-2} and 60 kW m^{-2} these cells went into thermal runaway at 182 and 55 seconds, respectively [30].

3. Experimental

The FTRC, depicted with Fig 1, is a specially designed calorimetric technique developed to provide insight into the heat output, mass ejections, and expelled gases that are generated due to Li-ion cell thermal runaway events; heat output can be analyzed in the form of total energy yield, fractional energy yield, heat rate, and heat flux. Additional benefits of the calorimeter include compatibility with interchangeable cell chambers to support testing of different cell types (see Fig 1c which depicts the cell chambers used for testing cylindrical cells), x-ray transparency for combination synchrotron experiments (refer to Fig 2), and rapid turnaround testing capability to provide the ability to collect statistically significant quantities of calorimetric data for thermal runaway characterization. The FTRC is also compatible with heater trigger and nail penetration trigger; see Fig 1c. The heater trigger mechanism can be combined with cells that have an internal short circuiting device installed to trigger the cells in a manner similar to an internal short. In general, the fractional calorimeter is used to characterize thermal runaway events for cells ranging up to 5 A-h in capacity, although research is currently underway for to develop

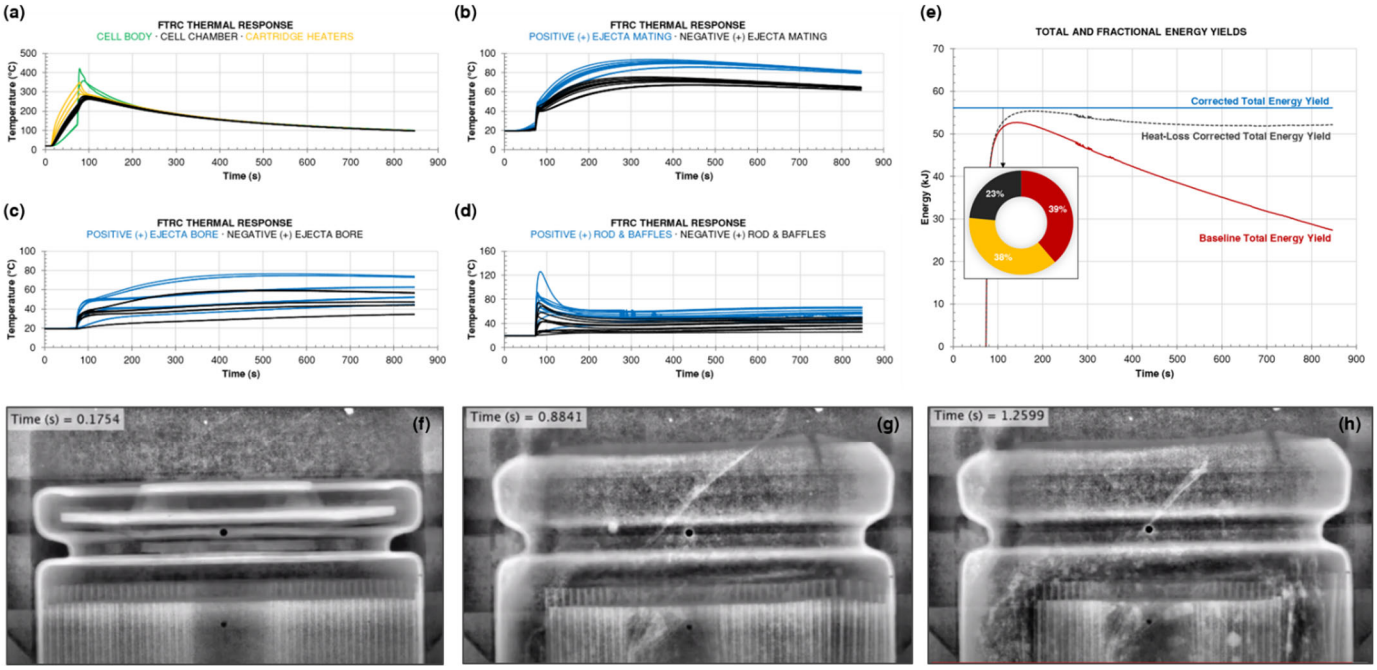

Fig 4 Image provides example FTRC dataset for a KULR 18650-K330 triggered into thermal runaway by combining the FTRC cartridge heaters with a K330 constructed with an internal short circuiting device installed. (a) displays the thermal response of the cell body, the cell chamber, and the cartridge heaters, (b) displays the thermal response of the positive and negative side ejecta mating assemblies, (c) displays the thermal response of the positive and negative side ejecta bore assemblies, and (d) displays the thermal response of the positive and negative side rod and baffle assemblies. Each line represents a thermocouple installed throughout the assembly. (e) displays the total energy yield and fractional energy yield. Additionally, (f)-(h) provide depiction of before, during, and after thermal runaway, respectively, as captured by high speed x-ray videography at DLS.

additional forms of fractional calorimetry to support pouch cells (referred to as P-FTRC) and large format cells with capacities that are greater than 100 A-h (referred to as L-FTRC) [31,32].

The FTRC has a centrally located cell chamber where the cell is installed and triggered into thermal runaway via one of the aforementioned trigger mechanisms. On both the positive and negative side of the calorimeter are identical ejecta mating assemblies, ejecta bore assemblies, and rod and baffle assemblies; refer to **Error! Reference source not found.**b. The symmetric design accommodates characterization of thermal runaway for cells with a bottom vent or for top vent cells that experience a bottom breach; refer to **Error! Reference source not found.**a. These assemblies are thermally isolated from the centrally located cell chamber with a low conductivity CoorsTek YTZP ceramic bushing (~2.2 W m^{-1} $°C^{-1}$) [33] which thermally isolates the energy released through the cell body from the energy released through the positive and negative side ejecta; refer to **Error! Reference source not found.**b. The ejecta mating assemblies will capture any large ejected electrode winding components that remain in-tact while the rod and baffle assemblies create a tortuous path which simultaneously decelerates the flow of the fine particulate and gases and extracts the associated heat of these components; see Fig 3.

Energy yield analysis of the data collected from the FTRC experiments allows for characterization of Li-ion cell thermal runaway response as a function of trigger mechanism and cell format. Total energy yield (kJ), fractional energy yield (kJ, %), heat rate (W), heat flux (W m^{-2}), and mass ejection distributions (g) are key measures in describing the violence of cell responses; note that Part 1 of this study focuses on the heat output variability, refer to Part 2 for description of relationships associated with thermal runaway mass ejections. Total energy yield describes the total heat release of a cell during a thermal runaway event while fractional energy yield describes the fraction of the total energy yield associated with heat release from the cell body, the positive end, and the negative end of the cell. The total energy yield is combined with the approximated length of the thermal runaway event to determine heat rate. Once heat rate is determined, it is combined with the surface area of the cell to determine the corresponding heat flux. Fig 4 provides depiction of an example fractional calorimetry thermocouple dataset for a KULR 18650-K330 and how that dataset is translated into the energy calculations that are recorded in the Battery Failure Databank. Additionally, extracts from the corresponding high speed X-ray video captured at the DLS facility in the UK are provided with Fig 4 to highlight the internal failure mechanisms of the cell before, during, and after thermal runaway.

A cell's thermal response to a given trigger mechanism is characterized with nearly 100 Type K thermocouples installed throughout the FTRC hardware. However, before performing any calculations, the thermocouple data is first examined for failures which may adversely affect or skew the energy yield calculations. Readings from failed thermocouples are corrected based on the response of neighboring thermocouples installed for redundancy.

After the thermocouple data is corrected for failures, the thermal runaway onset time is determined. The onset time represents the point at which thermal runaway is triggered in the cell, and is associated with a significant increase in temperature, as seen with the example in Fig 4a. This time is identified by observing a large and sudden increase in the temperature-time derivatives of the thermocouples installed on the lowest mass components (i.e. the FTRC baffles) and on the cell body. Since the FTRC energy calculations begin at the selected onset time, it is crucial that the earliest calculated onset value is selected to ensure that the energy yield of the entire event is reflected in the calculations.

The baseline total energy yield of is then determined through an energy balance equating the heat absorbed by the calorimeter to the energy released by due to thermal runaway. The heat absorbed by the calorimeter is calculated from thermocouple data, calorimeter

component masses and specific heats, and cell ejected mass. The baseline total energy yield, as calculated from the energy balance, is shown with Equation 1:

$$E_{baseline} = \sum m_i C_{p_i} dT_i \quad (1)$$

where $E_{baseline}$ represents baseline total energy yield (kJ), m represents mass (kg), C_p represents specific heat capacity (kJ kg^{-1} $°C^{-1}$), dT represents the change in temperature from the moment thermal runaway occurs (°C), and i represents the individual FTRC components, the cell body, and the ejecta material. An example of the transient change in baseline total energy yield throughout the course of a FTRC experiment is plotted with red line in Fig 4e.

While the baseline total energy yield provides an initial estimate of the energy released during a thermal runaway event, it does not account for the conductive heat losses from the calorimeter. Because a true adiabatic interface is not possible in a laboratory setting, the calorimeter loses some heat over the course of the experiment through conduction to its surrounding insulation. This causes the baseline total energy yield to slowly decrease when conductive heat loss rate exceeds the rate at which heat is absorbed from the thermal runaway event. It is important to consider the energy loss to the insulation, as neglecting it would underestimate the total heat released due to thermal runaway. Therefore, the conductive heat loss rate is determined for each experiment and is then used in the calculations to account for the heat loss to the calorimeter insulation over time using Equation 2:

$$E_{baseline+heat\,loss} = E_{baseline} + q_{insulation} t \quad (2)$$

where $E_{baseline+heat\,loss}$ represents the heat loss corrected total energy yield (kJ), $q_{insulation}$ represents the calorimeter's conductive heat loss rate (kJ s^{-1}), and t represents the time elapsed since the thermal runaway onset time (s). An example of the transient change in heat loss corrected total energy yield throughout the course of a FTRC experiment is plotted with gray dashed line in Fig 4e; note the flat line of the curve which represents what would have been observed in a true adiabatic testing environment.

The final step in determining the overall corrected total energy yield is to account for the heat associated with any unrecovered mass during the experiment. Following the law of conservation of mass, the total post-test mass (taken as the sum of the post-test cell mass and post-test ejecta mass) must equal the pre-test cell mass. However, throughout the course of the experiment small amounts of ejecta mass and vented gases can escape the system. To approximate the energy of the unrecovered mass, the cell failure mechanism is first determined. If the cell vented through its positive end, the unrecovered mass is assumed to have been ejected into the positive side of the calorimeter. If the cell vented through its negative end, the unrecovered mass is assumed to have been ejected into the negative side of the calorimeter. If the cell vented through both its positive and negative ends (or was a positive vent cell that experiences a bottom breach), the unrecovered mass is assumed to have been ejected equally into the positive and negative sides of the calorimeter. The maximum theoretical temperature change of the unrecovered mass is approximated based on the data collected from the corresponding baffle temperatures. The energy of the unrecovered mass for a given experiment is determined with Equation 3:

$$E_{unrecovered} = mC_p dT_{unrecovered\,(+)} + mC_p dT_{unrecovered\,(-)} \quad (3)$$

where $E_{unrecovered}$ represents the total unrecovered energy (kJ) and subscripts $+$ and $-$ refer to the positive and negative sides of the calorimeter, respectively.

Finally, the overall corrected total energy yield is determined as the sum of the heat loss corrected total energy yield and the energy of the unrecovered energy, as with Equation 4:

$$E_{corrected} = E_{baseline+heat\,loss} + E_{unrecovered} \quad (4)$$

where $E_{corrected}$ represents the overall corrected total energy yield (kJ). Note that the determination of the energy associated with the unrecovered mass is not a transient calculation but rather is determined as a single value. This value is added to the maximum value of the total baseline + heat loss corrected total energy yield curve as shown with the blue line in Fig 4e.

A key feature of the FTRC is that it also allows for discernment of fractional energy yields; that is, the fraction of the total energy released through the cell body vs. that of the ejected solids, liquids, and gases. By rewriting the energy balance in Equation 1, the baseline total energy yield can be represented as the sum of the cell body energy, positive side energy, and negative side energy:

$$E_{baseline} = \sum m_i C_{p_i} dT_{i_{body}} + \sum m_i C_{p_i} dT_{i_{pos}} + \sum m_i C_{p_i} dT_{i_{neg}} \quad (5)$$

where $body$ refers to the centrally located components used to capture the heat output of the cell body, pos refers to the positive side of the calorimeter, and neg refers to the negative side of the calorimeter. The ratios of the sum of the $body$ energies, the sum of the pos energies, and the sum of the neg energies to the baseline total energy yield at 15 seconds following the onset of thermal runaway is assumed to be representative of the distribution of the energy fractions; see pie chart example shown with Fig 4e. Note that the 15 second timeframe was identified as the optimal wait duration for enough thermal runaway heat to register as temperature rise on the FTRC components for the energy fractions to be determined, while also minimizing the amount of soak time that conductive losses could occur from the centrally located cell chamber to the positive and negative side ejecta mating assemblies.

It is assumed that the length of the thermal runaway event length can be characterized as the difference in time between the trigger of thermal runaway and when the lowest mass components of the calorimeter start cooling down (i.e. the cell itself and the internal aluminum baffles); see Section 4.3 for more detailed discussion on determination of event length. This approximated event length is combined with total energy yield to determine heat rate using the following equations:

$$q = \frac{\sum m_i C_{p_i} dT_i}{t_{event}} \quad 6a$$

$$q = \frac{E_{total}}{t_{event}} \quad 6b$$

where q is the rate event heat rate (W) and t_{event} is the approximated thermal runaway event length (s).

Once the heat rate is determined, the experiment heat flux may be determined. The calculation of heat flux is shown with the Equation 4:

$$Q = \frac{q}{A} \quad 7$$

where Q is the heat flux of the event (W m^{-2}) and A is the total surface area of the cell; Table 1 provides description of the total surface area for each cell type considered in this study.

4. Results

For this study, the KULR 18650-K330, KULR 21700-K500, LG 21700-M50, and Saft D-Cell-VES16 were tested in the FTRC with three trigger mechanisms; cartridge heaters, cartridge heaters plus an ISC device, and nail penetration; note that in the results cartridge heater trigger

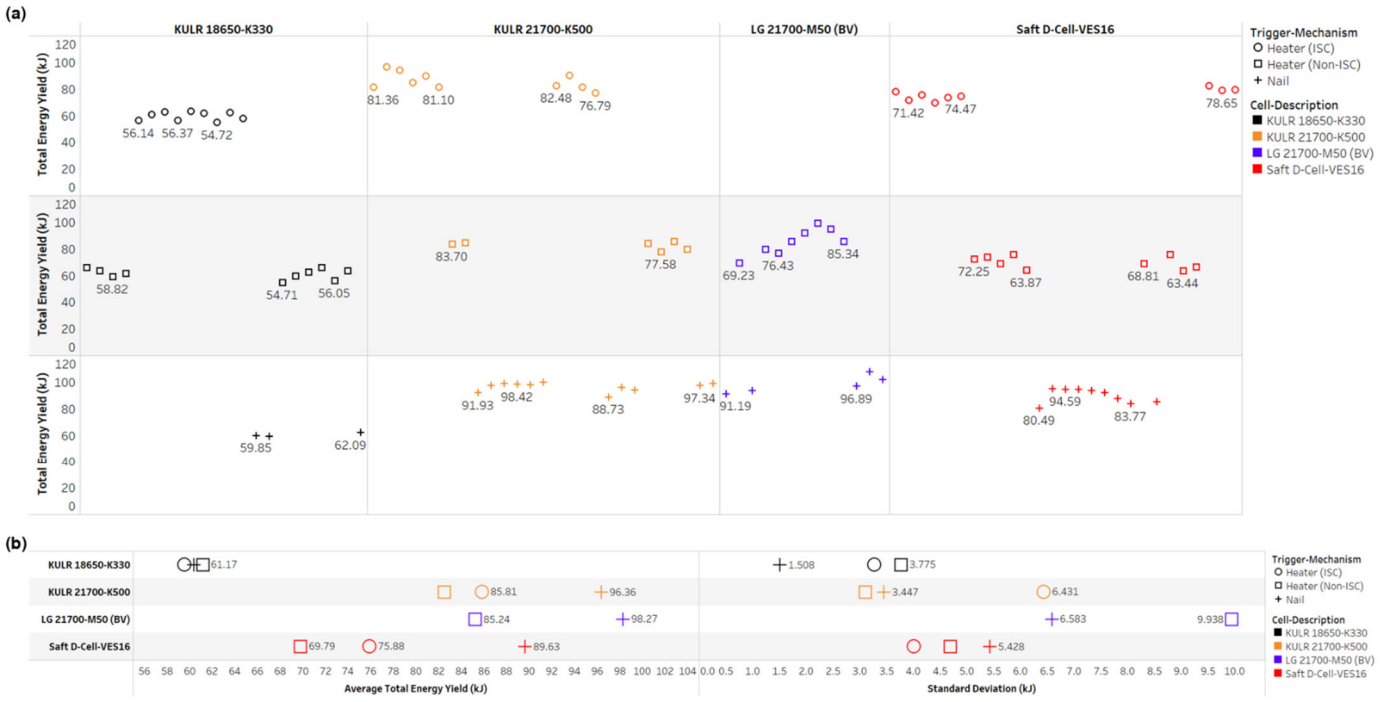

Fig 5 Plots characterize total energy yield as a function of cell format and trigger mechanism where (a) shows the test-to-test variability in total energy yield (note that the location on the x-axis is arbitrary) and where (b) shows the sample average total energy yield (left) and the associated standard deviation (right).

experiments are referred to as Heater (Non-ISC) trigger experiments and cartridge heater plus ISC trigger are referred to as Heater (ISC) experiments. Knowing that no two thermal runaway events are the same, up to 10 experiments for each cell format and trigger mechanism combination are conducted in order to capture the overall range of expected thermal runaway responses. Table 1 provides a description of the cells tested, their characteristics, the trigger mechanisms that were utilized, and the number of experiments that were conducted for each combination. Results are categorized based on comparison of total energy yield, fractional energy yield, heat rate, and heat flux.

For the KULR 18650-K300, 9 experiments were conducted using the Heater (ISC) trigger, 10 experiments were conducted using the Heater (Non-ISC) trigger, and 3 experiments were conducted using the Nail Penetration trigger. For the KULR 21700-K500, 10 experiments were conducted using the Heater (ISC) trigger, 6 experiments were conducted using the Heater (Non-ISC) trigger, and 11 experiments were conducted using the Nail Penetration trigger. For the LG 21700-M50, 7 experiments were conducted using the Heater (Non-ISC) trigger and 5 experiments were conducted using the Nail Penetration trigger. For the Saft D-Cell-VES16, 9 experiments were conducted using the Heater (ISC) trigger, 9 experiments were conducted using the Heater (Non-ISC) trigger, and 9 experiments were conducted using the Nail Penetration trigger.

4.1 Total Energy Yield Comparison

For the KULR 18650-K330 with Heater (ISC) trigger, the maximum observed thermal runaway energy yield was 63.3 kJ, the minimum was 54.7 kJ, the average was 59.6 kJ, and the standard deviation was 3.3 kJ. With the Heater (Non-ISC) trigger, the maximum was 65.7 kJ, the minimum was 54.7 kJ, the average was 61.2 kJ, and the standard deviation was 3.8 kJ. With the Nail Penetration trigger the maximum was 62.1 kJ, the minimum was 59.2 kJ, the average was 60.4 kJ, and the standard deviation was 1.5 kJ. The test-to-test total energy yields are compared with Fig 5a and the averages and standard deviations are compared with Fig 5b.

For the KULR 21700-K500 with Heater (ISC) trigger, the maximum observed thermal runaway energy yield was 96.4 kJ, the minimum was 76.8 kJ, the average was 85.8 kJ, and the standard deviation was 6.4 kJ. With the Heater (Non-ISC) trigger, the maximum was 85.6 kJ, the minimum was 77.6 kJ, the average was 82.5 kJ, and the standard deviation was 3.1 kJ. With the Nail Penetration trigger the maximum was 99.8 kJ, the minimum was 88.7 kJ, the average was 96.4 kJ, and the standard deviation was 3.4 kJ. The test-to-test total energy yields are compared with Fig 5a and the averages and standard deviations are compared with Fig 5b.

For the LG 21700-M50 with Heater (Non-ISC) trigger, the maximum was 99.0 kJ, the minimum was 69.2 kJ, the average was 85.2 kJ, and the standard deviation was 9.9 kJ. With the Nail Penetration trigger the maximum was 107.6 kJ, the minimum was 91.2 kJ, the average was 98.3 kJ, and the standard deviation was 6.6 kJ. The test-to-test total energy yields are compared with Fig 5a and the averages and standard deviations are compared with Fig 5b.

For the Saft D-Cell-VES16 with Heater (ISC) trigger, the maximum observed thermal runaway energy yield was 82.2 kJ, the minimum was 69.8 kJ, the average was 75.9 kJ, and the standard deviation was 4.0 kJ. With the Heater (Non-ISC) trigger, the maximum was 75.6 kJ, the minimum was 63.4 kJ, the average was 69.8 kJ, and the standard deviation was 4.7 kJ. With the Nail Penetration trigger the maximum was 94.8 kJ, the minimum was 80.5 kJ, the average was 89.6 kJ, and the standard deviation was 5.4 kJ. The test-to-test total energy yields are compared with Fig 5a and the averages and standard deviations are compared with Fig 5b.

There was not a significant difference in total heat output as a function of trigger mechanism for the KULR 18650-K330. The KULR 21700-K500 appeared to have an average of 12.3 % higher heat output for Nail Penetration vs. Heater (ISC) and a 16.8 % higher for Nail Penetration vs. heater (Non-ISC). The LG 21700-M50 has an average of 15.3 % higher heat output for Nail Penetration vs. Heater (Non-ISC). The

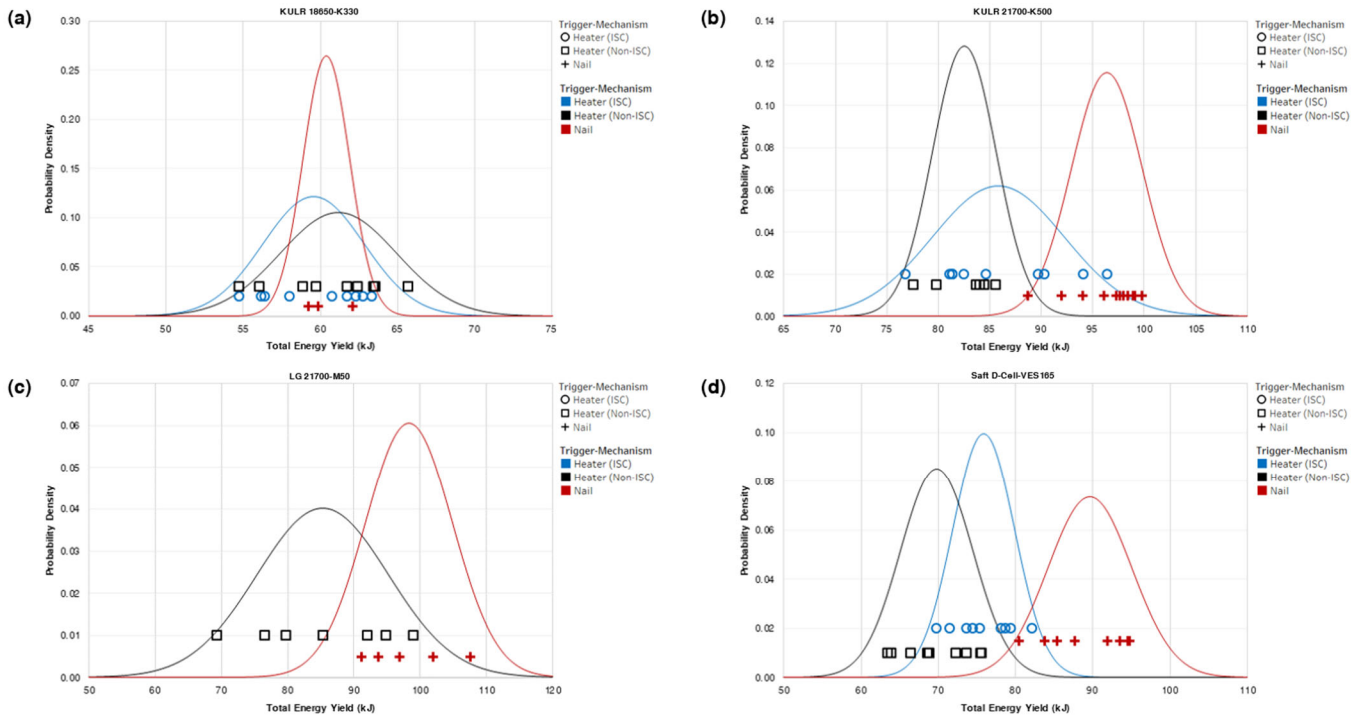

Fig 6 Plots characterize the normal probability density distribution for each cell type as a function of trigger mechanism where (a) shows the distributions for the KULR 18650-K330, (b) shows the distributions for the KULR 21700-K500, (c) shows the distributions for the LG 21700-M50, and (d) shows the distributions for the Saft D-Cell-VES16. For each distribution, the observed total energy yield datapoints that are used to generate the curve are arbitrarily plotted on the y-axis for visualization purposes. The peak of each curve represents the highest likelihood total energy yield for a given cell and trigger combination.

Saft D-Cell-VES16 had an average of 18.1 % higher heat output for Nail Penetration trigger vs. Heater (ISC) trigger and 28.4 % higher for Nail Penetration trigger vs. Heater (Non-ISC) trigger.

It is also helpful to consider thermal runaway as not just a singular value, but as a statistical distribution of probable events [11]. Previous studies indicated that thermal runaway total energy yield is best represented with a long right tail distribution, but that it could also be adequately represented with a normal distribution assumption [11]. Here we assume a normal distribution and provide comparison of the normal probability density distribution of each cell type as a function of trigger mechanism with Fig 6 which helps visualize the overall range of potential outcomes as a function of average and standard deviation.

The observed total energy yield datapoints that are used to generate the curves shown with Fig 6 are arbitrarily plotted on the y-axis for visualization purposes. In general, when evaluated along the x-axis with respect to the peak of the corresponding curve, the test-to-test variability in total energy release appears to be normally distributed (with the exception of the KULR 21700-K500 when triggered by nail which may be better characterized with a long left tail); this is in line with previous work reported by Walker et. al. [11]. The peak of each curve represents the highest likelihood total energy yield for a given cell and trigger combination and the span of each curve represents the corresponding theoretical range of total energy yield values.

The total energy yield of the KULR 18650-K330 did appear to have a strong correlation to trigger mechanism and any variation observed may well be within the error margin. Additionally, the KULR 18650-K330 total energy yield had lower overall test-to-test standard deviation, regardless of trigger mechanism, when compared to the LG 21700-M50 and the Saft D-Cell-VES16; the same is also true when comparing to the standard deviation of the KULR 21700-K500 Heater (ISC) experiments. Conversely, the larger cells tended to have higher standard deviations and to produce more heat output when triggered via nail penetration. On average, the KULR 21700-K500 nail penetration heat output was between 12.3 % and 16.8 % higher than the heater experiments, the LG 21700-M50 was 15.3 % higher than the heater experiments, and the Saft D-Cell-VES16 was between 18.1 % and 28.4 % higher than the heater experiments.

4.2 Fractional Energy Yield Comparison

In addition to total energy release, the FTRC also provides the ability to determine the fractional energy release by determining the energy change of components based on sub-assembly. Here we describe the fractional energy release for each cell type as a function of trigger mechanism.

For the KULR 18650-K330 with Heater (ISC) trigger, on average 21% of the 59.6 kJ total energy was released through the cell body, 32% through the positive side ejecta and gases, and 47% through the negative side ejecta and gases. With the Heater (Non-ISC) trigger, on average 30% of the 61.2 kJ total energy was released through the cell body, 24% through the positive side ejecta and gases, and 46% through the negative side ejecta and gases. With the Nail Penetration trigger, on average 34% of the 60.4 kJ total energy was released through the cell body, 46% through the positive side ejecta and gases, and 20% through the negative ejecta and gases. Fig 7a provides plots for the KULR 18650-K330 energy fractions as a function of trigger mechanism.

For the KULR 21700-K500 with Heater (ISC) trigger, on average 32% of the 85.8 kJ total energy was released through the cell body, 33% through the positive side ejecta and gases, and 35% through the negative side ejecta and gases. With the Heater (Non-ISC) trigger, on average 33% of the 82.5 kJ total energy was released through the cell body, 39% through the positive side ejecta and gases, and 28% through the negative side ejecta and gases. With the Nail Penetration trigger, on average 30% of the 96.4 kJ total energy was released through the cell body, 36% through the positive side ejecta and gases, and 34% through

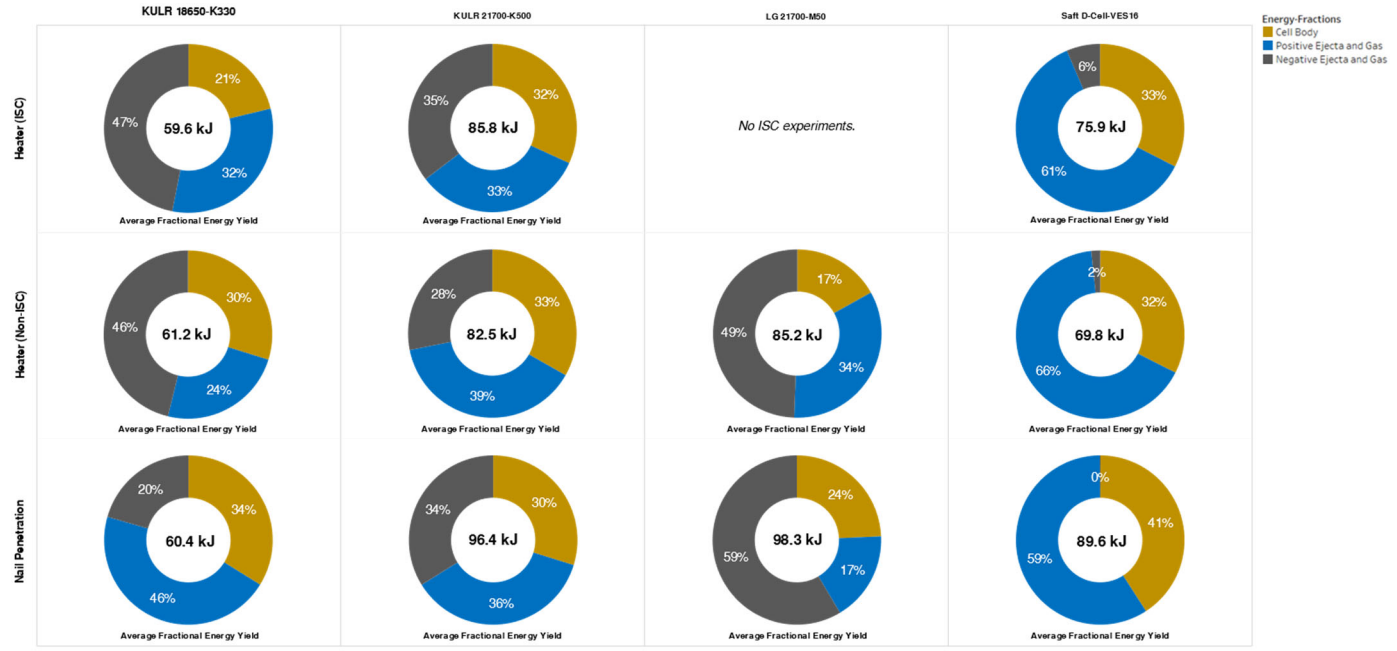

Fig 7 Comparison of the average fractional energy yield for each cell type and trigger mechanism configuration. Note that the average total energy yield for each configuration is annotated in the center of each pie chart.

the negative ejecta and gases. Fig 7b provides plots for the KULR 21700-K500 energy fractions as a function of trigger mechanism.

For the LG 21700-M50 with Heater (Non-ISC) trigger, on average 17% of the 85.2 kJ total energy was released through the cell body, 34% through the positive side ejecta and gases, and 49% through the negative side ejecta and gases. With the Nail Penetration trigger, on average 24% of the 98.3 kJ total energy was released through the cell body, 17% through the positive side ejecta and gases, and 59% through the negative ejecta and gases. Fig 7c provides plots for the LG 21700-M50 energy fractions as a function of trigger mechanism.

For the Saft-D-Cell-VES16 with Heater (ISC) trigger, on average 39% of the 75.9 kJ total energy was released through the cell body and 61% through the positive side ejecta and gases. With the Heater (Non-ISC) trigger, on average 34% of the 69.8 kJ total energy was released through the cell body and 66% through the positive side ejecta and gases. With the Nail Penetration trigger, on average 41% of the 89.6 kJ total energy was released through the cell body and 59% through the positive side ejecta and gases. Fig 7d provides plots for the Saft D-Cell-VES16 energy fractions as a function of trigger mechanism.

Other than for the KULR 21700-K500, nail penetration tended to result in the highest fraction of energy being released through the cell body. This is possibly because the nail traps a portion of the electrode winding assembly inside of the cell casing which forces the decomposition reactions to occur within the casing, which in turn means that a higher fraction of the total energy will be released through the cell body. When comparing the KULR 18650-K330 to the KULR 21700-K500, the 18650 variant appeared to have higher fractions of the total energy release coming through the negative side of the cell when compared to the 21700 variant which maintained a relatively even distribution of the fractions regardless of trigger mechanism. Note that even though the Saft D-Cell-VES16 is a top vent cell (i.e. no bottom vent), there is still a small fraction of the energy released through the negative side of the cell. There are four potential causes for this: (1) heat radiating from the bottom surface, (2) bottom rupture events, (3) hot gases escaping from the cell chamber through the negative end of the FTRC, and (4) no system is truly adiabatic and there could be some small levels of heat loss from the cell chamber to the positive and negative side ejecta mating assemblies.

4.3 Heat Rate Comparison

While it is important to understand the variability in thermal runaway energy release and energy fractions, it is equally important to characterize the experiment-to-experiment heat rate (W) and heat flux (W cm^{-2}); refer to Equations 6 & 7. To determine heat-rate, and subsequently heat flux, one must first know the associated length of the thermal runaway event for a given experiment.

To determine the length of each experiment, we evaluated the transient temperature response of the lowest mass components of the FTRC; i.e. the temperatures as characterized by the cell body thermocouples and the positive and negative side baffle thermocouples. The transient thermal response was evaluated for each of these components from the moment of thermal runaway trigger until the point of inflection, or when the component starts cooling down. The assumption is that the temperatures of the low mass components will trend upward (i.e. heating) as long as an active heat flux is applied and that they will trend downward (i.e. cooling) as soon as the active heat flux subsides. This moment of inflection is assumed to be the approximate *end* of the event. The difference in time between the inflection point and the moment of trigger is considered to be the length of the event.

For each experiment the maximum time to inflection, minimum time to inflection, and average time to inflection (average of the maximum and minimum values) is determined based on the responses of the thermocouples installed on the cell body, the positive baffles, and the negative baffles. These values are combined with test-to-test total energy yields to determine the range of corresponding heat rates and heat fluxes.

The maximum heat rate is achieved by dividing total energy yield by the shortest possible event length, the minimum heat rate is determined by dividing by the longest possible event length, and the average heat rate is determined by dividing by the average event

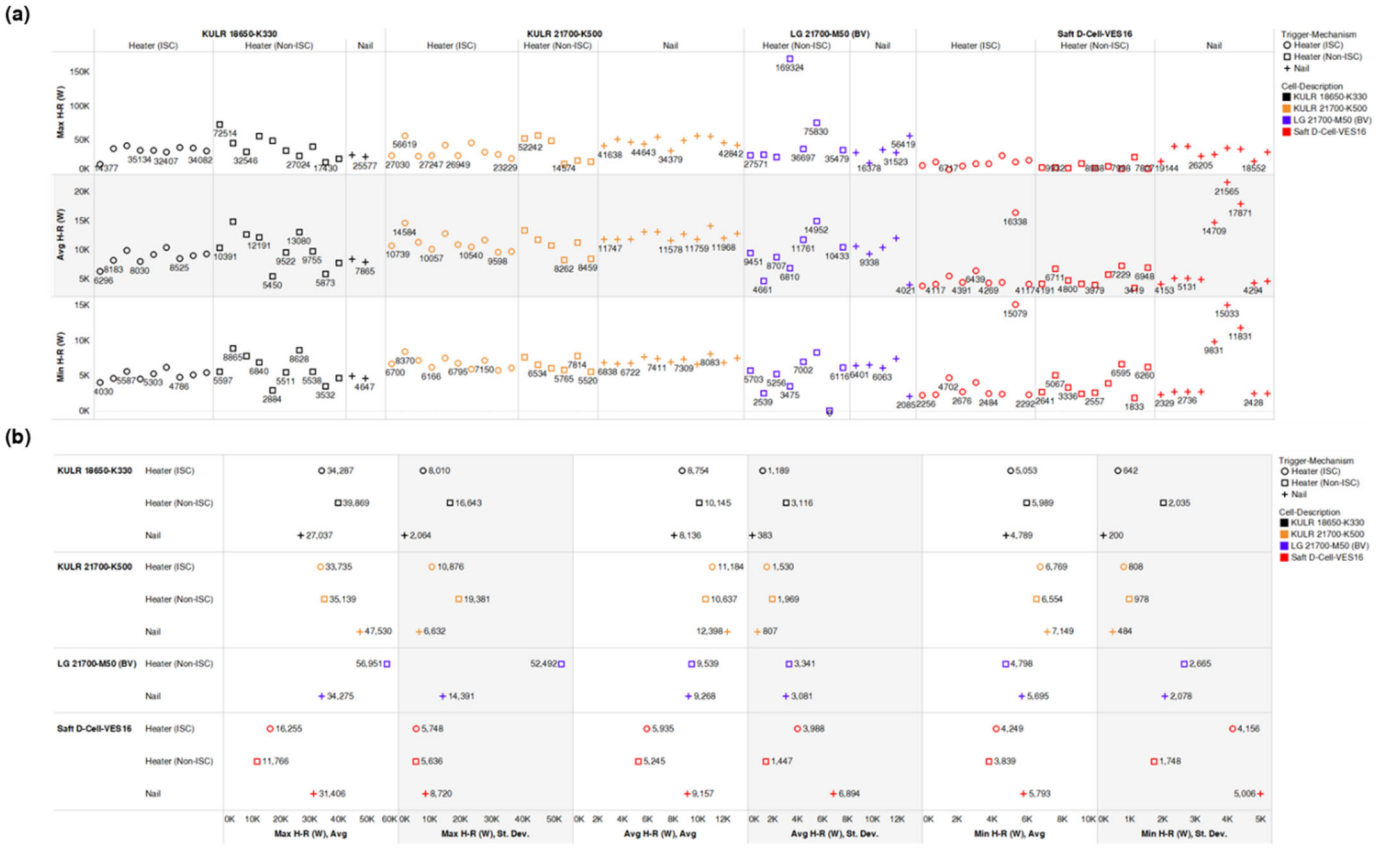

Fig 8 Plots characterize thermal runaway heat rate (W) as a function of cell format and trigger mechanism where (a) shows the test-to-test variability in heat rate (note that the location on the x-axis is arbitrary) and where (b) shows the overall average heat rates and standard deviations.

length. These test-to-test heat rates for each cell type and trigger mechanism combination are compared with the plots in Fig 8a and the overall averages and standard deviations are compared with the plots in Fig 8b.

For the KULR 18650-K330 Heater (ISC) experiments, the max possible heat rate ranged between 14.4 kW and 41.8 kW with an average of 34.3 kW and an associated standard deviation of 8.0 kW. The average possible heat rate ranged between 6.3 kW and 10.3 kW with an average of 8.7 kW and an associated standard deviation of 1.9 kW. The min possible heat rate ranged between 4.0 kW and 6.2 kW with an average of 5.1 kW and an associated standard deviation of 0.6 kW.

For the KULR 18650-K330 Heater (Non-ISC) experiments, the max possible heat rate ranged between 17.4 kW and 72.5 kW with an average of 39.9 kW and an associated standard deviation of 16.6 kW. The average possible heat rate ranged between 5.5 kW and 14.8 kW with an average of 10.6 kW and an associated standard deviation of 2.0 kW. The min possible heat rate ranged between 2.9 kW and 8.9 kW with an average of 6.0 kW and an associated standard deviation of 2.0 kW.

For the KULR 18650-K330 Nail Penetration experiments, the max possible heat rate ranged between 25.6 kW and 28.5 kW with an average of 27.0 kW and an associated standard deviation of 2.1 kW. The average possible heat rate ranged between 7.9 kW and 8.4 kW with an average of 8.1 kW and an associated standard deviation of 0.4 kW. The min possible heat rate ranged between 4.6 kW and 4.9 kW with an average of 4.8 kW and an associated standard deviation of 0.2 kW.

For the KULR 21700-K500 Heater (ISC) experiments, the max possible heat rate ranged between 23.2 kW and 56.6 kW with an average of 33.7 kW and an associated standard deviation of 10.9 kW. The average possible heat rate ranged between 9.6 kW and 14.6 kW with an average of 11.2 kW and an associated standard deviation of 1.5 kW. The min possible heat rate ranged between 5.8 kW and 8.4 kW with an average of 6.8 kW and an associated standard deviation of 0.8 kW.

For the KULR 21700-K500 Heater (Non-ISC) experiments, the max possible heat rate ranged between 14.6 kW and 56.3 kW with an average of 35.1 kW and an associated standard deviation of 19.4 kW. The average possible heat rate ranged between 8.3 kW and 13.4 kW with an average of 10.6 kW and an associated standard deviation of 2.0 kW. The min possible heat rate ranged between 5.5 kW and 7.8 kW with an average of 6.6 kW and an associated standard deviation of 1.0 kW.

For the KULR 21700-K500 Nail Penetration experiments, the max possible heat rate ranged between 34.4 kW and 56.4 kW with an average of 47.5 kW and an associated standard deviation of 6.6 kW. The average possible heat rate ranged between 9.6 kW and 14.6 kW with an average of 12.4 kW and an associated standard deviation of 0.8 kW. The min possible heat rate ranged between 6.6 kW and 8.1 kW with an average of 7.1 kW and an associated standard deviation of 0.5 kW.

For the LG 21700-M50 Heater (Non-ISC) experiments, the max possible heat rate ranged between 25.4 kW and 169.3 kW with an average of 57.0 kW and an associated standard deviation of 52.5 kW. The average possible heat rate ranged between 4.7 kW and 15.0 kW with an average of 9.5 kW and an associated standard deviation of 3.3 kW. The min possible heat rate ranged between 2.5 kW and 8.3 kW with an average of 4.8 kW and an associated standard deviation of 2.7 kW.

For the LG 21700-M50 Nail Penetration experiments, the maximum possible heat rate ranged between 16.4 kW and 56.4 kW with an average of 34.3 kW and an associated standard deviation of 14.4 kW. The average possible heat rate ranged between 4.0 kW and 12.0 kW with an average of 9.3 kW and an associated standard deviation of 3.1 kW. The minimum possible heat rate ranged between 2.1 kW and 7.4

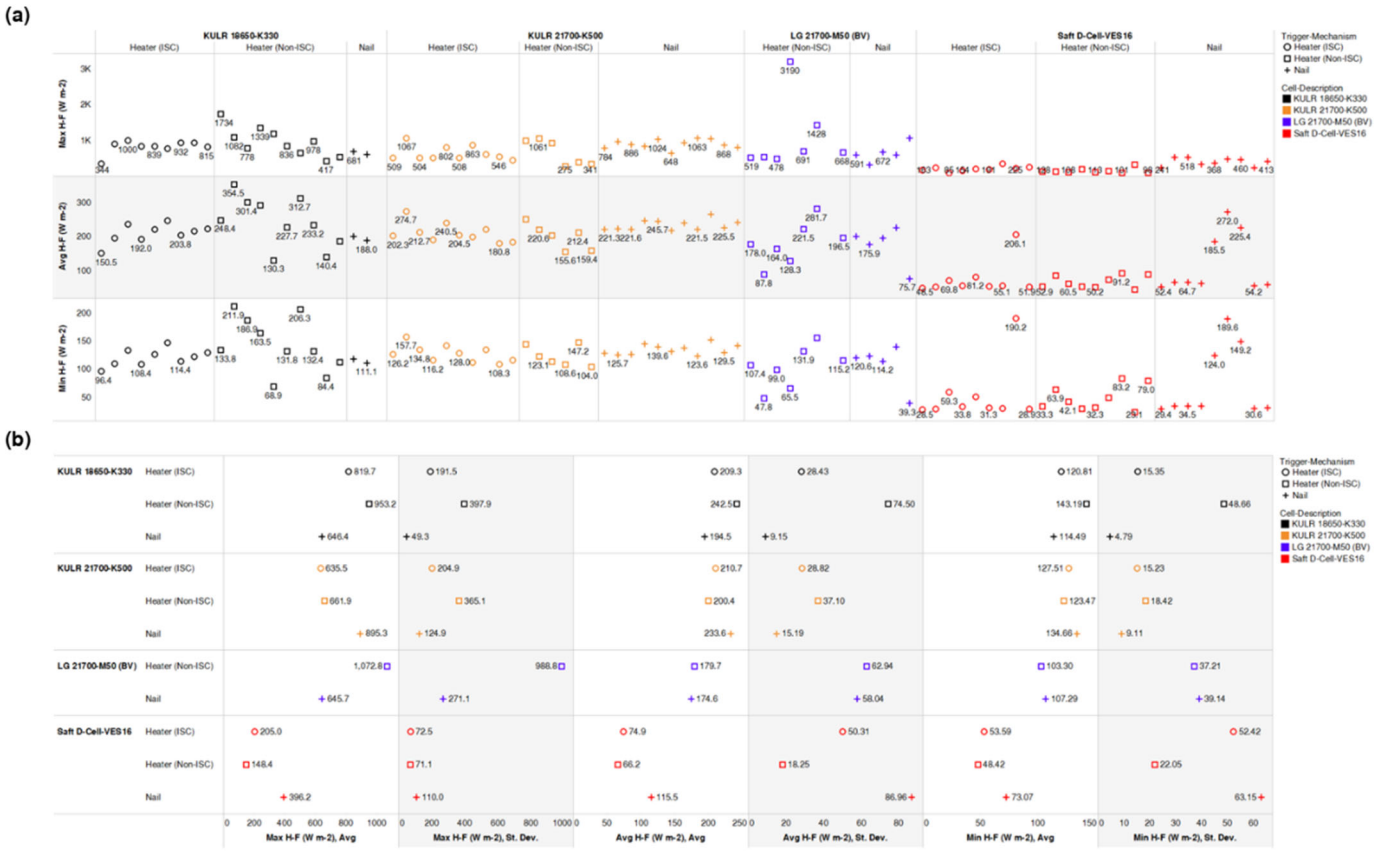

Fig 9 Plots characterize thermal runaway heat flux (W m^{-2}) as a function of cell format and trigger mechanism where (a) shows the test-to-test variability in heat flux (note that the location on the x-axis is arbitrary) and where (b) shows the overall average heat fluxes and standard deviations.

kW with an average of 5.7 kW and an associated standard deviation of 2.1 kW.

For the SAFT D-CELL-VES16 Heater (ISC) experiments, the max possible heat rate ranged between 6.7 kW and 27.3 kW with an average of 16.3 kW and an associated standard deviation of 5.7 kW. The average possible heat rate ranged between 3.8 kW and 16.3 kW with an average of 5.9 kW and an associated standard deviation of 4.0 kW. The min possible heat rate ranged between 2.3 kW and 15.1 kW with an average of 4.2 kW and an associated standard deviation of 4.2 kW.

For the SAFT D-CELL-VES16 Heater (Non-ISC) experiments, the max possible heat rate ranged between 7.8 kW and 25.3 kW with an average of 11.8 kW and an associated standard deviation of 5.6 kW. The average possible heat rate ranged between 3.4 kW and 7.2 kW with an average of 5.2 kW and an associated standard deviation of 1.4 kW. The min possible heat rate ranged between 1.8 kW and 6.6 kW with an average of 3.8 kW and an associated standard deviation of 1.7 kW.

For the SAFT D-CELL-VES16 Nail Penetration experiments, the max possible heat rate ranged between 18.6 kW and 41.1 kW with an average of 31.4 kW and an associated standard deviation of 8.7 kW. The average possible heat rate ranged between 4.2 kW and 21.6 kW with an average of 9.2 kW and an associated standard deviation of 6.9 kW. The min possible heat rate ranged between 2.3 kW and 15.0 kW with an average of 5.8 kW and an associated standard deviation of 5.0 kW.

4.4 Heat Flux Comparison

Building from heat rate, heat flux may also be analyzed; refer to Equation 7. To determine heat flux the heat rates described in Section 4.3 are divided by the total surface area for each cell as reported in Table 1; for the KULR 18650-K330 this is 41.8 cm^2, for the KULR 21700-K500 this is 46.2 cm^2, for the LG 21700-M50 this is 46.2 cm^2, and for the Saft D-Cell-VES16 this is 79.3 cm^2. The test-to-test heat fluxes for each cell type and trigger mechanism combination are compared with the plots in Fig 9a and the overall averages and standard deviations are compared with the plots in Fig 9b.

For the KULR 18650-K330 Heater (ISC) experiments, the max possible heat flux ranged between 344 W cm^{-2} and 1000 W cm^{-2} with an average of 820 W cm^{-2} and an associated standard deviation of 192 W cm^{-2}. The average possible heat flux ranged between 151 W cm^{-2} and 247 W cm^{-2} with an average of 209 W cm^{-2} and an associated standard deviation of 28 W cm^{-2}. The min possible heat flux ranged between 96 W cm^{-2} and 147 W cm^{-2} with an average of 121 W cm^{-2} and an associated standard deviation of 15 W cm^{-2}.

For the KULR 18650-K330 Heater (Non-ISC) experiments, the max possible heat flux ranged between 417 W cm^{-2} and 1734 W cm^{-2} with an average of 953 W cm^{-2} and an associated standard deviation of 398 W cm^{-2}. The average possible heat flux ranged between 130 W cm^{-2} and 355 W cm^{-2} with an average of 243 W cm^{-2} and an associated standard deviation of 75 W cm^{-2}. The min possible heat flux ranged between 69 W cm^{-2} and 212 W cm^{-2} with an average of 143 W cm^{-2} and an associated standard deviation of 49 W cm^{-2}.

For the KULR 18650-K330 Nail Penetration experiments, the max possible heat flux ranged between 611 W cm^{-2} and 681 W cm^{-2} with an average of 646 W cm^{-2} and an associated standard deviation of 49 W cm^{-2}. The average possible heat flux ranged between 188 W cm^{-2} and 201 W cm^{-2} with an average of 195 W cm^{-2} and an associated standard deviation of 9 W cm^{-2}. The min possible heat flux ranged between 111 W cm^{-2} and 118 W cm^{-2} with an average of 114 W cm^{-2} and an associated standard deviation of 5 W cm^{-2}.

For the KULR 21700-K500 Heater (ISC) experiments, the max possible heat flux ranged between 438 W cm^{-2} and 1067 W cm^{-2} with an average of 636 W cm^{-2} and an associated standard deviation of 205 W cm^{-2}. The average possible heat flux ranged between 181 W cm^{-2} and 275 W cm^{-2} with an average of 211 W cm^{-2} and an associated standard deviation of 29 W cm^{-2}. The min possible heat flux ranged between 108 W cm^{-2} and 158 W cm^{-2} with an average of 128 W cm^{-2} and an associated standard deviation of 15 W cm^{-2}.

For the KULR 21700-K500 Heater (Non-ISC) experiments, the max possible heat flux ranged between 275 W cm^{-2} and 1061 W cm^{-2} with an average of 662 W cm^{-2} and an associated standard deviation of 365 W cm^{-2}. The average possible heat flux ranged between 156 W cm^{-2} and 252 W cm^{-2} with an average of 200 W cm^{-2} and an associated standard deviation of 37 W cm^{-2}. The min possible heat flux ranged between 104 W cm^{-2} and 147 W cm^{-2} with an average of 123 W cm^{-2} and an associated standard deviation of 18 W cm^{-2}.

For the KULR 21700-K500 Nail Penetration experiments, the max possible heat flux ranged between 648 W cm^{-2} and 1063 W cm^{-2} with an average of 895 W cm^{-2} and an associated standard deviation of 125 W cm^{-2}. The average possible heat flux ranged between 218 W cm^{-2} and 266 W cm^{-2} with an average of 234 W cm^{-2} and an associated standard deviation of 15 W cm^{-2}. The min possible heat flux ranged between 124 W cm^{-2} and 152 W cm^{-2} with an average of 135 W cm^{-2} and an associated standard deviation of 9 W cm^{-2}.

For the LG 21700-M50 Heater (Non-ISC) experiments, the max possible heat flux ranged between 478 W cm^{-2} and 3190 W cm^{-2} with an average of 1073 W cm^{-2} and an associated standard deviation of 989 W cm^{-2}. The average possible heat flux ranged between 88 W cm^{-2} and 282 W cm^{-2} with an average of 180 W cm^{-2} and an associated standard deviation of 63 W cm^{-2}. The min possible heat flux ranged between 48 W cm^{-2} and 156 W cm^{-2} with an average of 103 W cm^{-2} and an associated standard deviation of 37 W cm^{-2}.

For the LG 21700-M50 Nail Penetration experiments, the max possible heat flux ranged between 309 W cm^{-2} and 1063 W cm^{-2} with an average of 646 W cm^{-2} and an associated standard deviation of 271 W cm^{-2}. The average possible heat flux ranged between 76 W cm^{-2} and 226 W cm^{-2} with an average of 175 W cm^{-2} and an associated standard deviation of 58 W cm^{-2}. The min possible heat flux ranged between 39 W cm^{-2} and 139 W cm^{-2} with an average of 107 W cm^{-2} and an associated standard deviation of 39 W cm^{-2}.

For the SAFT D-Cell-VES16 Heater (ISC) experiments, the max possible heat flux ranged between 85 W cm^{-2} and 344 W cm^{-2} with an average of 205 W cm^{-2} and an associated standard deviation of 73 W cm^{-2}. The average possible heat flux ranged between 49 W cm^{-2} and 206 W cm^{-2} with an average of 75 W cm^{-2} and an associated standard deviation of 50 W cm^{-2}. The min possible heat flux ranged between 29 W cm^{-2} and 190 W cm^{-2} with an average of 54 W cm^{-2} and an associated standard deviation of 52 W cm^{-2}.

For the SAFT D-Cell-VES16 Heater (Non-ISC) experiments, the max possible heat flux ranged between 98 W cm^{-2} and 320 W cm^{-2} with an average of 148 W cm^{-2} and an associated standard deviation of 71 W cm^{-2}. The average possible heat flux ranged between 43 W cm^{-2} and 91 W cm^{-2} with an average of 66 W cm^{-2} and an associated standard deviation of 18 W cm^{-2}. The min possible heat flux ranged between 23 W cm^{-2} and 83 W cm^{-2} with an average of 48 W cm^{-2} and an associated standard deviation of 22 W cm^{-2}.

For the SAFT D-Cell-VES16 Nail Penetration experiments, the max possible heat flux ranged between 234 W cm^{-2} and 518 W cm^{-2} with an average of 396 W cm^{-2} and an associated standard deviation of 110 W cm^{-2}. The average possible heat flux ranged between 52 W cm^{-2} and 272 W cm^{-2} with an average of 116 W cm^{-2} and an associated standard deviation of 87 W cm^{-2}. The min possible heat flux ranged between 29 W cm^{-2} and 190 W cm^{-2} with an average of 73 W cm^{-2} and an associated standard deviation of 63 W cm^{-2}.

Overall, the max observed heat fluxes ranged from 1734 W cm-2 to 3190 W cm^{-2} depending on the cell being analyzed. For comparison, the Apollo crew capsule could experience up to 800 W cm^{-2} peak heating rates when re-entering Earth's atmosphere at the completion of a given mission [34,35]. This puts into perspective the level of thermal protection and/or vent path design that may be required to protect Li-ion battery assemblies and their surroundings from the immediate torching effect that occurs when a cell experiences thermal runaway. In some cases, ablative technology may offer solutions for mitigating the impact of thermal runaway torching effects.

4.5 Comparison of Heat Rate, Heat Flux, and Total Energy Yield

Additional analysis was conducted to compare the experiment to experiment heat rates and heat fluxes to the corresponding total energy yield values. Fig. 10a compares the corresponding heat rate and total energy yield values on an experiment to experiment basis and Fig. 10b compares the same on an average to average basis. Additionally, Fig. 10c compares the corresponding heat flux and total energy yield values on an experiment to experiment basis and Fig. 10d compares the same on an average to average basis.

A relationship between trigger mechanism and cell format may be apparent when evaluating heat rate vs. total energy yield as a function of trigger mechanism. As seen with the averages in Fig. 10b, heat rate tended to be the highest for the Nail Penetration and Heater (ISC) triggers and lowest for the Heater (Non-ISC) triggers for the 21700 and D-Cell format Li-ion cells. Also shown with Fig. 10b, the 18650 format Li-ion cell (i.e. the KULR K330) Heater (Non-ISC) experiments tended to result in both the highest average total energy yield and highest average heat rate, the Nail Penetration experiments tended to result in the middle average total energy yield (of the three trigger mechanisms), but the lowest average heat rate, and the Heater (ISC) experiments resulted in the lowest average total energy yield and the middle average heat rate (of the three trigger mechanism). Each of these identified relationships stand true for the comparison of total energy yield to heat flux as well.

The LG 21700-M50 tended to be the most inconsistent when attempting to compare total energy yield with heat rate and heat flux. Additionally, the test-to-test standard deviations for total energy yield and fractional energy yield were the highest when compared to the other cell types. These differences could be attributed yes, to chemistry differences, but also to the differences in the mechanical design features of the cell. A given cell casing with an associated thickness, vent path, and burst pressure may result in a propensity for a cell to fail one way vs. another (e.g. nominal failure vs. bottom breach vs. spin groove breach vs. side wall rupture) and it is these differences in failure that have been reported to impact the energy yield [11]. Further investigation of the influences of specific mechanical design features on the thermal runaway behavior of a cell may be warranted.

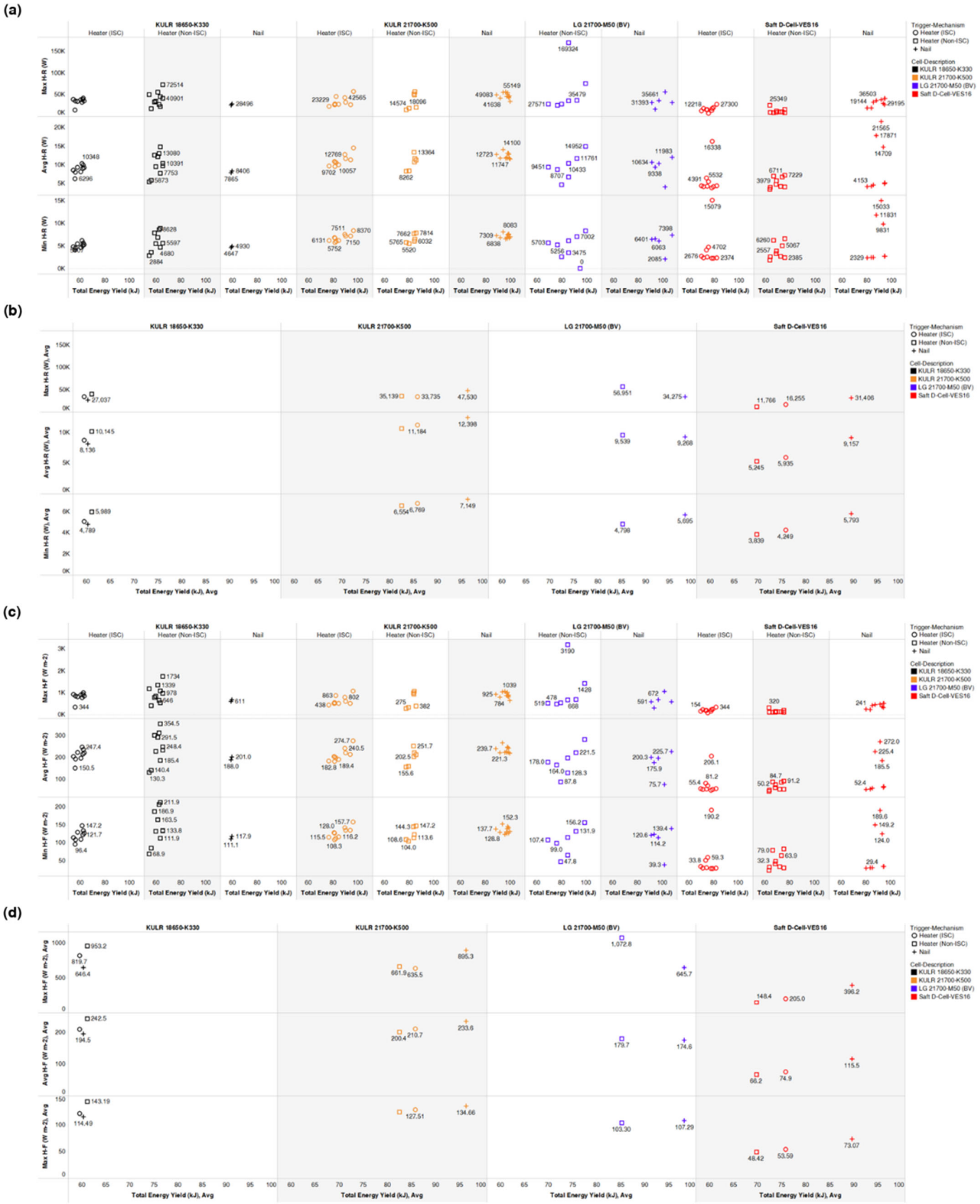

Fig 10 Comparison of heat rate, heat flux, and total energy yield where (a) compares experiment to experiment total energy yield and heat rate values, (b) compares average total energy yield and average heat rate values, (c) compares experiment to experiment total energy yield and heat flux values, and (d) compares average total energy yield and average heat flux values.

5. Conclusions

Lithium-ion (Li-ion) technology is a popular energy storage solution utilized across industries for its high energy density and low mass. With a range of formats and designs for both high power and high energy applications, Li-ion cells are versatile and configurable. Despite their widespread popularity, there are major safety concerns regarding their potential for explosive and violent thermal runaway (TR) events. The potential for such catastrophic failures necessitates safe battery design with robust thermal management systems. However, to achieve these goals often complex thermal modelling and extensive abuse testing campaigns are required to certify batteries for usage in their intended applications. There is a need to understand the impacts of trigger mechanism and cell format on thermal runaway heat output in order to improve testing capabilities and better inform thermal models.

This study examines thermal runaway heat output for three different cell formats as a function of trigger mechanism. The cell formats considered are 18650, 21700, D-cell. The trigger mechanisms considered are heaters, internal short circuiting (ISC) device, and nail penetration. Specifically, the thermal runaway responses for the KULR 21700-K500, KULR 21700-K500, LG 21700-M50, and Saft D-Cell-VES16 are examined. All experiments are conducted inside of a FTRC. The FTRC data, which is stored in the Battery Failure Databank, is extracted and analyzed to provide a comparative analysis of thermal runaway heat output as a function of trigger mechanism and cell format based on the calculated total energy yield, fractional energy yield, rate of heat flow, and heat flux. By analyzing the experiment to experiment variability in these values, this study seeks to demonstrate relationships between thermal runaway heat output, cell format, and initiation method to aid in the development of future abuse tests and modeling methods.

This study reveals that, for larger cells, Nail Penetration trigger mechanism tends to result in higher thermal runaway heat output. In the case of the KULR 21700-K500, this resulted in TBD% higher heat output when compared to Heater (ISC) and TBD% higher heat output when compared to Heater (Non-ISC). For the LG 21700-M50, this resulted in TBD% higher heat output when compared to Heater (Non-ISC). For the Saft D-Cell-VES16, this resulted in TBD% higher heat output when compared to Heater (ISC) and TBD% higher heat output when compared to Heater (Non-ISC). Additionally, the nail penetration experiments also tended to result in higher fractions of the total energy being released through the cell body when compared to the other trigger mechanisms; the only exception was the KULR 21700-K500. It is possible that this higher fraction of energy is related to the nail constraining more of the electrode winding material to remain inside of the cell casing thereby forcing the decomposition reactions to occur within the cell casing; and subsequently higher fractions of the total energy are released through the cell casing.

This study also demonstrates successful translation of FTRC results, as captured by the Battery Failure Databank, into meaningful analysis that breaks down the influence of specific conditions on thermal runaway heat output; in this case cell format vs. trigger mechanism. Additional studies could be conducted with the FTRC to evaluate the influence of other variables on the total and fractional thermal runaway heat output such as cell chemistry, cell capacity, casing thickness, internal burst pressure, and state-of-charge. State-of-charge based studies using accelerating rate calorimetry are very prominent in literature and may be greatly supplemented with the inclusion of fractional heat output vs. state-of-charge [26,36]. Examination of thermal runaway behavior as a function of cathode material is also commonly found in literature and, if conducted, similar studies using FTRC may reveal new insights in this regard [37].

Acknowledgements

This work was authored by collaborators from the National Aeronautics and Space Administration (NASA) Johnson Space Center, the Universities Space Research Association (USRA), Jacobs, the National Renewable Energy Laboratory (NREL), and the University College London (UCL). These experiments were performed between beamlines ID19 at the European Synchrotron Radiation Facility (ESRF) in Grenoble, France and at the I12 at Diamond Light Source (DLS) Facility in Harwell, UK. We are grateful to the ESRF and Diamond Light Source for allowing us to use their facilities. Special acknowledgement is given to Zoran Bilc who assisted the collaborators for this study in assembling hardware prior to all test series conducted at the synchrotron facilities.

References

1. Zubi, G., Dufo-López, R., Carvalho, M. & Pasaoglu, G. The lithium-ion battery: State of the art and future perspectives. *Renewable and Sustainable Energy Reviews* (2018) doi:10.1016/j.rser.2018.03.002.
2. Bandhauer, T. M., Garimella, S. & Fuller, T. F. A Critical Review of Thermal Issues in Lithium-Ion Batteries. *J. Electrochem. Soc.* **158**, R1 (2011).
3. Liu, H., Wei, Z., He, W. & Zhao, J. Thermal issues about Li-ion batteries and recent progress in battery thermal management systems: A review. *Energy Convers. Manag.* **150**, 304–330 (2017).
4. Doughty, D. H. & Roth, E. P. A General Discussion of Li Ion Battery Safety. *Interface Mag.* **21**, 37–44 (2012).
5. Balakrishnan, P. G., Ramesh, R. & Prem Kumar, T. Safety Mechanisms in Lithium-Ion Batteries. *J. Power Sources* **155**, 401–414 (2006).
6. Feng, X. *et al.* Thermal runaway mechanism of lithium ion battery for electric vehicles: A review. *Energy Storage Materials* (2018) doi:10.1016/j.ensm.2017.05.013.
7. Yayathi, S., Walker, W. Q., Doughty, D. H. & Ardebili, H. Energy distributions exhibited during thermal runaway of commercial lithium ion batteries used for human spaceflight applications. *J. Power Sources* **329**, (2016).
8. Walker, W. Q. *Rechargeable lithium batteries for aerospace applications*. *Rechargeable Lithium Batteries: From Fundamentals to Applications* (2015). doi:10.1016/B978-1-78242-090-3.00014-6.
9. *Aircraft Incident Report Auxiliary Power Unit Battery Fire Japan Airlines Boeing 787-8, JA829J Boston, Massachusetts January 7, 2013*. (2013).
10. Quintiere, J. G., Crowley, S. B., Walters, R. N., Lyon, R. E. & Blake, D. *Fire Hazards of Lithium Batteries*. (2016).
11. Walker, W. Q. *et al.* Decoupling of heat generated from ejected and non-ejected contents of 18650-format lithium-ion cells using statistical methods. *J. Power Sources* **415**, 207–218 (2019).
12. Coman, P. T., Rayman, S. & White, R. E. A Lumped Model of Venting During Thermal Runaway in a Cylindrical Lithium Cobalt Oxide Lithium-Ion Cell. *J. Power Sources* **307**, 56–62 (2016).
13. Finegan, D. P. *et al.* Tracking Internal Temperature and Structural Dynamics during Nail Penetration of Lithium-Ion Cells. *J. Electrochem. Soc.* **164**, A3285–A3291 (2017).
14. Finegan, D. P. *et al.* Investigating lithium-ion battery materials during overcharge-induced thermal runaway: An operando and multi-scale X-ray CT study. *Phys. Chem. Chem. Phys.* **18**,

30912–30919 (2016).
15. Lamb, J., Orendorff, C. J., Steele, L. A. M. & Spangler, S. W. Failure propagation in multi-cell lithium ion batteries. *J. Power Sources* **283**, 517–523 (2015).
16. Lopez, C. F., Jeevarajan, J. A. & Mukherjee, P. P. Experimental Analysis of Thermal Runaway and Propagation in Lithium-Ion Battery Modules. *J. Electrochem. Soc.* **162**, A1905–A1915 (2015).
17. Srinivasan, R. *et al.* Preventing Cell-to-Cell Propagation of Thermal Runaway in Lithium-Ion Batteries. *J. Electrochem. Soc.* **167**, 020559 (2020).
18. Finegan, D. P. *et al.* In-operando high-speed tomography of lithium-ion batteries during thermal runaway. *Nat. Commun.* **6**, 1–10 (2015).
19. Rickman, S. L. *et al.* Considerations for the Thermal Modeling of Lithium-Ion Cells for Battery Analysis. in *46th International Conference on Environmental Systems* 1–16 (2016).
20. Finegan, D. P. *et al.* Identifying the Cause of Rupture of Li-Ion Batteries during Thermal Runaway. *Adv. Sci.* 1700369 (2017) doi:10.1002/advs.201700369.
21. Finegan, D. P. D. P. *et al.* Modelling and experiments to identify high-risk failure scenarios for testing the safety of lithium-ion cells. *J. Power Sources* **417**, 29–41 (2019).
22. Finegan, D. P. *et al.* Characterising thermal runaway within lithium-ion cells by inducing and monitoring internal short circuits. *Energy Environ. Sci.* **10**, 1377–1388 (2017).
23. Walker, W. Q. *et al.* Battery Failure Databank. in *National Aeronautics and Space Administration* (National Aeronautics and Space Administration).
24. Lyon, R. E. & Walters, R. N. Energetics of lithium ion battery failure. *J. Hazard. Mater.* (2016) doi:10.1016/j.jhazmat.2016.06.047.
25. Zhao, C., Sun, J. & Wang, Q. Thermal runaway hazards investigation on 18650 lithium-ion battery using extended volume accelerating rate calorimeter. *J. Energy Storage* **28**, (2020).
26. Golubkov, A. W. *et al.* Thermal runaway of commercial 18650 Li-ion batteries with LFP and NCA cathodes – impact of state of charge and overcharge. *RSC Adv.* **5**, 57171–57186 (2015).
27. Jhu, C.-Y., Wang, Y. W., Shu, C. M., Chang, J. C. & Wu, H. C. Thermal explosion hazards on 18650 lithium ion batteries with a VSP2 adiabatic calorimeter. *J. Hazard. Mater.* **192**, 99–107 (2011).
28. Liu, X. *et al.* Heat release during thermally-induced failure of a lithium ion battery: Impact of cathode composition. *Fire Saf. J.* (2016) doi:10.1016/j.firesaf.2016.08.001.
29. Lammer, M., Königseder, A. & Hacker, V. Holistic methodology for characterisation of the thermally induced failure of commercially available 18650 lithium ion cells. *RSC Adv.* **7**, 24425–24429 (2017).
30. Fu, Y. *et al.* An experimental study on burning behaviors of 18650 lithium ion batteries using a cone calorimeter. *J. Power Sources* **273**, 216–222 (2015).
31. Pham, M. T. M. *et al.* Correlative acoustic time-of-flight spectroscopy and X-ray imaging to investigate gas-induced delamination in lithium-ion pouch cells during thermal runaway. *J. Power Sources* (2020) doi:10.1016/j.jpowsour.2020.228039.
32. Rickman, S. L. *et al. Calorimetry for Large-format Lithium-ion Cell Thermal Runaway (TR) Volume II : GS Yuasa 134-Ah Cell Testing Summary*. vol. II (2020).
33. *YTZP Chemistry Data Sheet*. (2012).
34. Laub, B. & Venkatapathy, E. Thermal Protection System Technology and Facility Needs for Demanding Future Planetery Missions. in *Planetary Probe Atmospheric Entry and Dscent Trajectory Analysis and Science2* (European Space Agency, 2003).
35. Pavlosky, J. E. & St Leger, L. G. *Apollo Experience Report - Thermal Protection Subsystem*. (1974).
36. Kvasha, A. *et al.* A comparative study of thermal runaway of commercial lithium ion cells. *Energy* (2018) doi:10.1016/j.energy.2018.06.173.
37. Peng, P. & Jiang, F. Thermal safety of lithium-ion batteries with various cathode materials: A numerical study. *Int. J. Heat Mass Transf.* (2016) doi:10.1016/j.ijheatmasstransfer.2016.07.088.